Delft University of Technology

Bending study of submarine power cables based on a repeated unit cell model

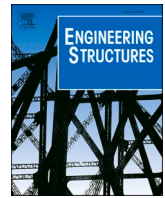Fang, Pan; Li, Xiao; Jiang, Xiaoli; Hopman, Hans; Bai, Yong

Important note
To cite this publication, please use the final published version (if applicable).
Please check the document version above.

Bending study of submarine power cables based on a repeated unit cell model

Pan Fang [a,1,*], Xiao Li [b,1,*], Xiaoli Jiang [a], Hans Hopman [a], Yong Bai [c]

[a] *Department of Maritime and Transport Technology, Delft University of Technology, Netherlands*
[b] *Institute of High Performance Computing (IHPC), Agency for Science, Technology and Research (A*STAR), 1 Fusionopolis Way, #16-16 Connexis, Singapore 138632, Republic of Singapore*
[c] *College of Civil Engineering and Architecture, Zhejiang University, Hangzhou, Zhejiang, China*

ABSTRACT

Predicting the bending behaviours of a submarine power cable (SPC) is always a tough task due to its complex geometry and inner layer contact, not to mention the stick–slip mechanism. A full-scale finite element model is cumbersome during the early design stage and a more efficient model for practical use is required. Therefore, in this paper, a repeated unit cell (RUC) technique-based FE model is developed, which simplifies the bending analysis of SPCs using a short-length representative cell with periodic conditions. The verification of this RUC model is conducted from cable and component levels, respectively. The cable overall response is validated by the curvature-moment relationships from our cable bending tests regarding four cable samples whose material properties are obtained through a set of material tests. As for the component level, the behaviours of particular components are studied and compared with the results from a full-scale numerical model. Discrepancy is observed between the RUC model and the test, which can be explained by the distinctions of boundary conditions between these two methods. The proposed Cable-RUC model has been found robust and computationally efficient for studying SPCs under bending.

1. Introduction

The floating offshore renewable energy (ORE) industry is increasingly recognized as a crucial contributor to the global clean energy supply, offering a viable alternative to conventional energy sources. Its role in providing a substantial amount of clean energy continues to grow steadily. The existing available floating ORE includes wind energy, wave energy and tidal energy, etc. Among these, offshore wind energy is a young industry that began in 1991 when the first wind farm was installed off the Danish coast [1]. One of the immature technologies in this industry is the dynamic submarine power cables (SPC) that connect the power grid. SPCs experience various loadings during both deployment and operation phases, including axisymmetric loadings such as tension, torsion, external pressure and bending. For example, during the installation process, SPCs are subjected to combined tension and bending [2]. During their operational lifespan, they endure continuous dynamic cyclic loading, particularly cyclic bending and tension [3]. This kind of loading during operation could expose SPCs to a high risk of

fatigue failure that could be predicted and avoided based on the study of the cables' mechanical behaviour. Even though studies regarding SPCs under axisymmetric loadings appeared recently [4,5], there is no enough research about their bending behaviour, and it is hard to find relevant information from specific SPC standards – such as from ISO 13628–5 [6], DNV-RP-F401 [7].

SPCs are a type of contact-intensive structure characterized by multiple layers and materials, where the majority of components remain unbonded, as exemplified by the three-core SPC depicted in Fig. 1. Understanding the behaviour of SPCs presents significant challenges, primarily due to the intricate helical structures within their armour layer. This armour layer serves as a vital mechanical component, granting the organism the necessary flexibility for optimal performance. Under axisymmetric loadings, the assumption that the helical wires can be simulated via beam element has been proved acceptable [4,5]. This assumption greatly enhances the calculation speed, reaching levels that would be otherwise unimaginable, particularly when dealing with sufficiently long samples. Yet in bending simulation, contact issue plays a key role in its overall behaviour, thus the helical wires are no longer

---

Nomenclature

ORE	Offshore renewable Energy
SPC	Submarine Power Cable
RUC	Repeated Unit Cell
MPC	Multi-point Constraint
RP	Reference Point
DOF	Degree of Freedom
XDPE	Cross-linked Polyethylene
MDPE	Medium-density Polyethylene
R_B	Bending radius of the cable
φ	Rotation angle
ϕ	Rotation vector
$\mathbf{R}(\phi)$	Rotation matrix
$\mathbf{X},X$	Coordinate vector and its component
$\mathbf{U}, u$	Displacement vector and its component
ε	Strain
σ	Stress
L	Cable length

|	
α	Winding angle of wires
E	Young's Modulus
μ	Poisson's Ratio
A	Cross section area of a wire
κ	Cable curvature
V	Wire location along the cross section
V^*	Critical transition angle between stick and slip area
r	Radius of the helical layer
M	Bending moment
ε_e	Elastic strain
ε_p	Plastic strain
K	Nonlinear modulus
g	the hardening exponent
F	Axial force
L_{RUC}	Length of the RUC model
p	Wire pitch length
m	Number of wires
r,r_0,r_1,r_2,r_3	Coefficient of quaternion parameter representation
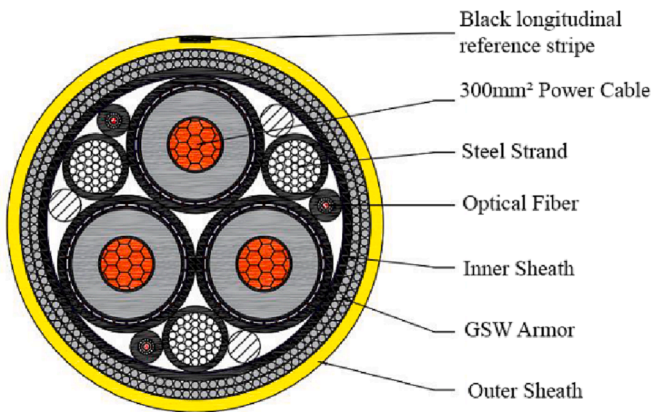
Fig. 1. A typical three-core SPC.

suitable to be simulated by beam element. A traditional way to deal with this is to replace the beam element with another element that is able to capture the contact situation, such as the classical solid element[8]. However, this poses a huge challenge for the simulation because a sample from a bending test is normally quite long [9–12] and thus contains huge amount of elements. The calculation in this case is usually time-consuming and involves serious convergence issue, which makes the simulation challenging and full of uncertainties during the early design stage. Therefore, a reliable and efficient simulation model requiring less computational cost is in demand.

A model as short as possible with less elements has the potential to solve the demand by taking advantage of the particular structure features of the components inside a SPC. The structure can be reduced to a very short length based on the homogenization method [13–16]. The starting point of this method is to offer an efficient and rigorous mean for reducing the size of the domain by cautiously taking care of the boundary conditions. These models have also been extended into flexible pipes [17–19], with prescribed requirements about wire number and pitch length. Based on the homogenization method, repeated unit cell (RUC) model has also been proposed and applied in flexible pipes and SPCs [20–23]. However, the kinematic restraints caused by the large curvature influence of the cable are not presented clearly in the previous studies. In addition, the material nonlinearity is not considered, and no experimental method is used to validate their model.

This paper aims to propose a fundamental RUC model to predict the bending stiffness of SPCs by achieving a balance between efficiency and accuracy. Therefore, the loading type for the models in this study is limited to bending moment. The methodology encompassing the test, RUC model and the full-scale model is given in Fig. 2. The full-scale model termed in this paper is a long model whose length is determined according to Paumier[24]. RUC model, the key delivery of this
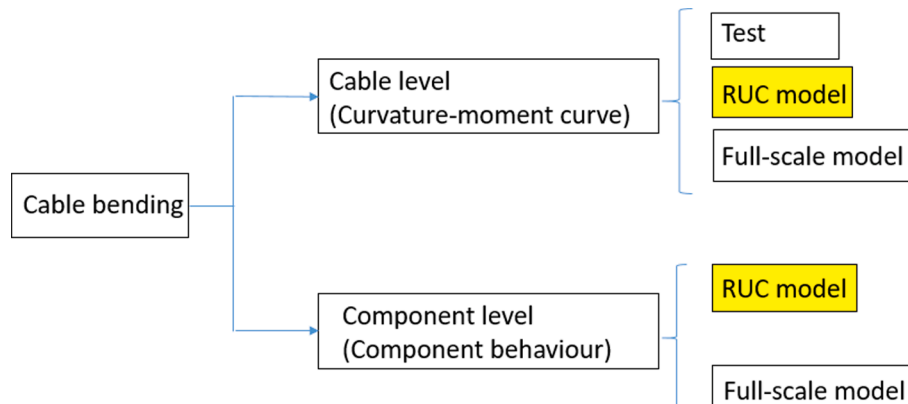

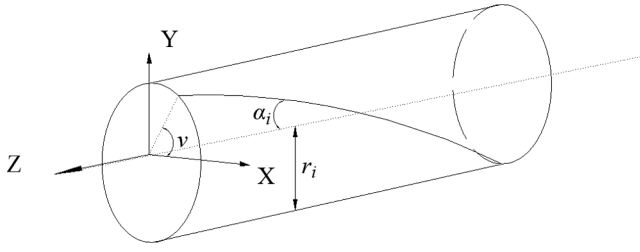**Fig. 2.** The methodology of the verification of the Cable-RUC model.
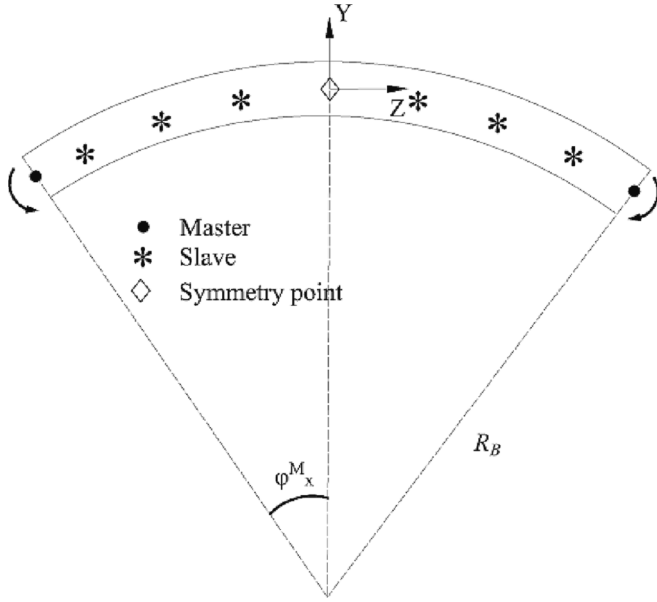
Fig. 3. Helical wire on a cylinder.

Fig. 4. Illustration of loading situation.

paper, is validated against the test results and verified through the full-scale model on the cable level. The component behaviours such as the displacement of the helical wire layer are verified through the full-scale model as well. The RUC model is introduced in Section 2. Following that, Section 3 details a series of tests employed for acquiring material properties and validating the RUC model through a comparison of the curvature-moment relationship. Section 4 outlines a full-scale numerical model with proper boundary conditions. Section 5 presents a case study regarding the power cable sample from Section 3. The results form a solid basis for the study of the overall SPCs.

2. Development of RUC model

RUC is a technique which utilizes the periodic boundary condition to reduce the cable length in numerical modelling [25]. The length of an RUC model is decided by the wire pitch length (p) and the wire number (m), given by the equation below:

$$L_{\text{RUC}} = \frac{p}{m} = \frac{2\pi r_i}{m \tan \alpha_i} \tag{1}$$

The parameters r_i and α_i are illustrated in Fig. 3. For numerical reasons outlined in the next section, to make the centre plane as a symmetry plane, the RUC model is extended symmetrically to a length of $2L_{\text{RUC}}$.

2.1. Model configuration

The layers inside the cables can be categorized into two types according to their structural configurations: cylinder/tubular layers and

the helical wire layers. The RUC model is proposed to deal with real power cables under bending where a constant curvature is assumed on the cylinder layers. This will be given in detail in section 2.1.1. Then the periodic boundary conditions for the helical wire layer will be introduced in section 2.1.2.

2.1.1. Constant curvature for the bent cable

In order to simulate the bending behaviour by the RUC model, the curvature is assumed to be constant over the cable. The basic idea of forming the constant curvature can be illustrated in Fig. 4. As long as the reference points (RPs) in the cable centreline coupled to the corresponding cross section move in a certain way, the whole structure will achieve a constant curvature. The detailed coupling setup of these RPs is clarified in Section 2.2.2. Specifically, the degree of freedoms (DOFs) of all the RPs should be set in the following way, where U1, U2 & U3 are the translational DOFs in X, Y& Z direction, respectively, and U4, U5 & U6 are the rotational DOFs.

- The symmetry point is fixed in all DOFs to avoid rigid body motion since it is in the symmetric plane.
- U1, U5 and U6 of the master RPs are restricted, while a rotation angle φ_x^{M} is applied in the U4 direction.
- U1, U5 and U6 of the slave RPs are all restricted, while the other DOFs are calculated based on the movement of the corresponding master RP. The calculation is automatically finished by building a series of multi-point constraint (MPC) user-subroutine in ABAQUS. The introduction to this user subroutine and the implementation of the MPC are outlined below.

According to Diehl [26] and Abaqus [27], for ABAQUS to process a user-defined MPC, three components are supposed to be supplied:

a. A matrix of DOF identifiers, JDOF(MDOF,N).
b. Matrices representing derivatives of the constraint function regarding the nodal DOFs.
c. The formulas expressing the movements of the slave DOFs based on the movements of the master DOF.

The main tasks are finding the constraint equations for corresponding DOFs of the nodes involved in the user-defined MPC, and then transforming them into the three components that ABAQUS requires.

As long as rotation angles are applied on the two master RPs, the bending radius R_B can be expressed as:

$$R_B = \frac{X_z^{\text{M}} + u_z^{\text{M}}}{\sin \varphi_x^{\text{M}}} \tag{2}$$

where X, u and φ are the initial coordinate, displacement and rotation angle, respectively. The superscript M denotes master RP while the subscripts mean the coordinate axes. Then the displacement of the master RP in the Y direction is:

$$f_1\left(u_y^{\text{M}}, \varphi_x^{\text{M}}\right) = u_y^{\text{M}} - R_B\left(1 - \cos \varphi_x^{\text{M}}\right) = 0 \tag{3}$$

Then the movement of the slave RPs can be calculated according to the maser RP's displacement, and the movement of the RPs are:

$$\varphi_x^{\text{S}} = \varphi_x^{\text{M}} \frac{X_z^{\text{S}}}{X_z^{\text{M}}} \tag{4}$$

$$u_y^{\text{S}} = R_B\left(1 - \cos \varphi_x^{\text{S}}\right) \tag{5}$$

$$u_z^{\text{S}} = R \sin \varphi_x^{\text{S}} - X_z^{\text{S}} \tag{6}$$

where the superscript S denotes the slave node. Again, Eq. (4), Eq. (5) and Eq. (6) can be rewritten according to the form of the user subroutine MPC:
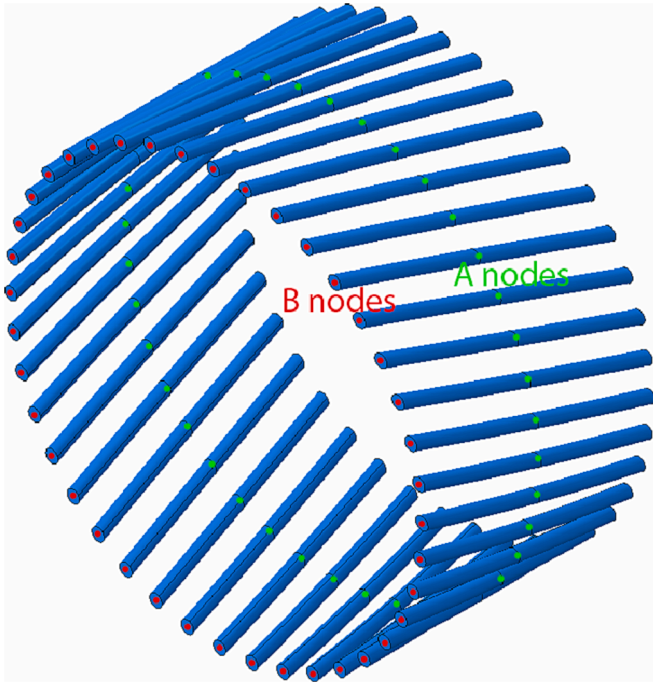
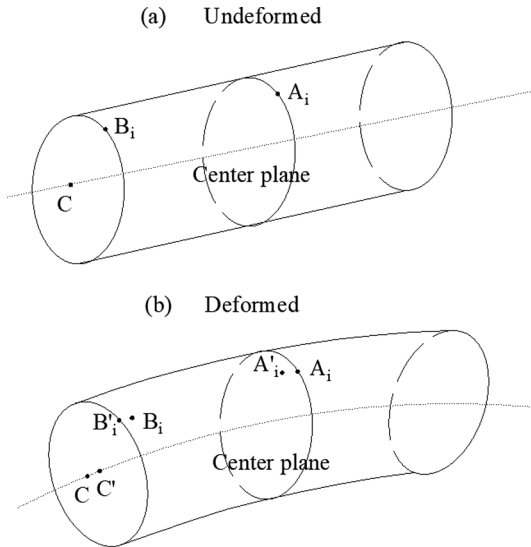**Fig. 5.** Nodes involved in periodicity conditions on the helical wire layer.

(a)   Undeformed

(b)   Deformed

Fig. 6. (a) Undeformed and (b) deformed configuration illustrating the location of the nodes A_i, B_i and C.

$$f_1\left(\varphi_x^S, \varphi^M\right) = \varphi_x^S - \varphi_x^M \frac{X_z^S}{X_z^M} = 0 \tag{7}$$

$$f_2\left(u_y^S, u_z^M, \varphi^M\right) = u_y^S - R_B\left(1 - \cos\varphi_x^S\right) = 0 \tag{8}$$

$$f_3\left(u_z^S, u_x^M, \varphi^M\right) = u_z^S + X_z^S - R_B\sin\varphi_x^S = 0 \tag{9}$$

By inputting the partial derivatives of the constraint functions involving corresponding DOFs into the ABAQUS subroutine, a constant curvature can be achieved.

2.1.2. Periodic condtions for the helical wire layer

After dealing with the cylinder structure, the next step is to take care of the movement of the wires in the RUC model. The basic ideas of the
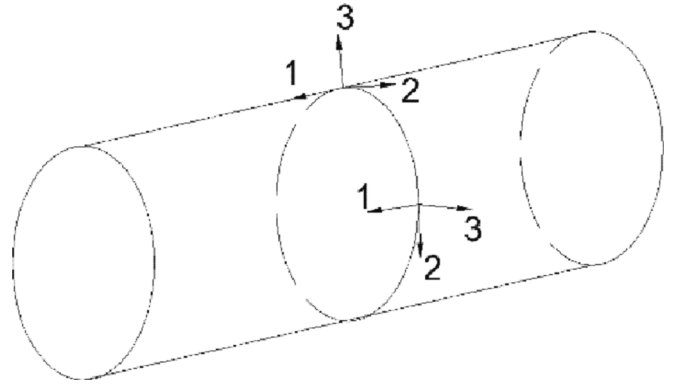

Fig. 7. Local coordinate system for a single wire.

periodic coupling setting-up of the wires will be illustrated and outlined in this section by considering the large curvature influence of the cable.

As mentioned before, to make the centre plane a symmetry plane in the axial direction, the RUC model is extended symmetrically to a length of $2L_{\text{RUC}}$. Due to the symmetry property, a group of B nodes on the left edge and a group of A nodes in the middle plane are illustrated for the explanation, as shown in Fig. 5, where A_i and B_i are the corresponding A node and B node on the same generatrix. The nodes on the right edge should be tackled the same way. The corresponding A node and B node on the same generatrix are coupled with the left master RP, denoted as C in the middle of left cross section, in which way the DOFs of nodes B are eliminated by the periodic constraint while nodes A and the master RP C remain unaffected as the controlling nodes. This constraint is implemented in ABAQUS by the MPC user subroutine as well. The following gives the derivation of the constraint equations.

The three groups of nodes A, B and C aforementioned satisfy a particular kinetic relation during the bending process, as illustrated by Fig. 6 where the three nodes on an undeformed and deformed configuration are given, respectively. The original letters without a superscript denote the initial node while the letters with the superscript represent the node after deformation. According to Caleyron, F., et al. and Leroy, J.-M., et al. [20,21], the kinetic relation among these three nodes after deformation based on a rigid body rotation can be expressed by:

$$\overrightarrow{C'B_i} = R(\phi^C)\left(\overrightarrow{CB_i} + \overrightarrow{A_iA_i'}\right), \phi^C = \left[\varphi_x^C \ \varphi_y^C \ \varphi_z^C\right] \tag{10}$$

where φ_x^C, φ_y^C and φ_z^C are the rotation angles of the master RP around X, Y and Z axis, respectively. $R(\phi^C)$ is the rotation matrix at point C. Now denoting the coordinates of A, B and C as $\mathbf{X^A}$, $\mathbf{X^B}$ and $\mathbf{X^C}$, respectively, which are the knowns imported into the MPC user subroutine. Then the coordinate of A$'$, B$'$ and C$'$ can be described by $\mathbf{X^A} + \mathbf{U^A}, \mathbf{X^B} + \mathbf{U^B}$ and $\mathbf{X^C} + \mathbf{U^C}$, respectively. Here **U** is the displacement of each node. Therefore, Eq. (10) can be rewritten as:

$$X^B + U^B - X^C - U^C = R(\phi^C)(X^B - X^C + X^A + U^A - X^A) \tag{11}$$

Eq. (11) can be reorganized according to the MPC form as:

$$f(U^B, U^A, U^C) = X^B + U^B - X^C - U^C - R(\phi^C)(X^B - X^C + U^A) = 0 \tag{12}$$

The derivation of the coefficient written in the MPC subroutine can be achieved by partial derivatives over the displacements of each node. It is clear that with respect to nodes A, B and C:

$$A^A = \frac{\partial f}{\partial U^A} = -R(\phi^C) \tag{13}$$

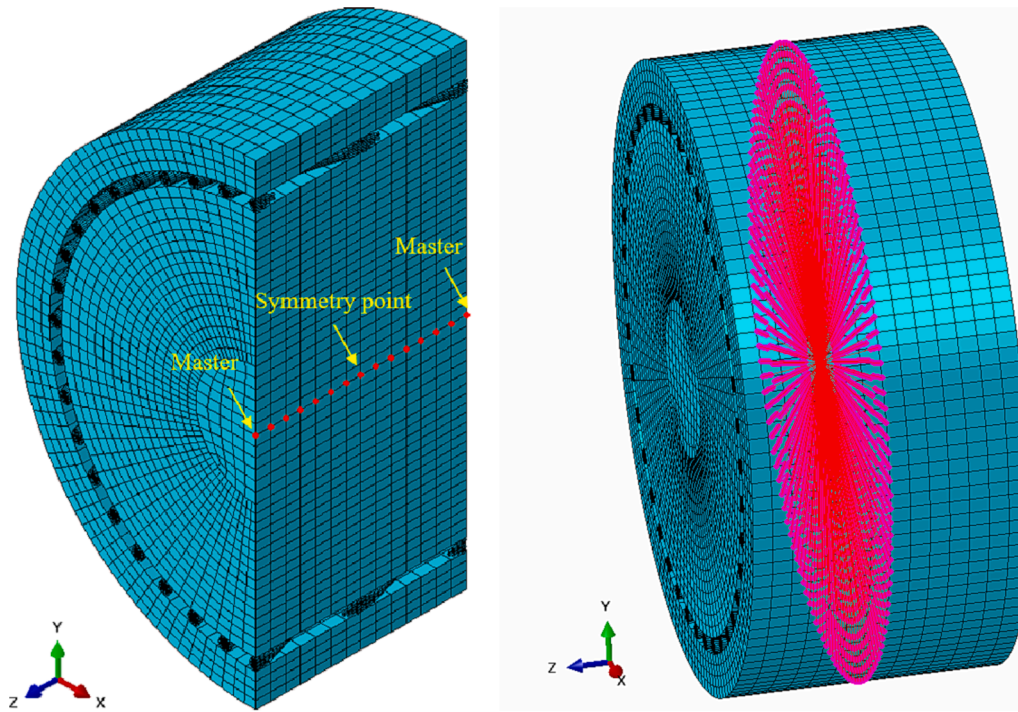$$A^B = \frac{\partial f}{\partial U^B} = I \tag{14}$$

Fig. 8. The controlling nodes in the centreline of Layer I (left) and a coupling illustration in the symmetric plane (right).

Table 1
Coupling DOFs of the points.

	Master						Symmetry point						Slave					
	U1	U2	U3	U4	U5	U6	U1	U2	U3	U4	U5	U6	U1	U2	U3	U4	U5	U6
Layer I	0	0	1	1	0	0	0	0	1	1	0	0	0	0	1	1	0	0
Layer II	0	0	1	1	0	0	0	0	1	1	0	0	0	0	0	0	0	0
Layer IV	0	0	1	1	0	0	0	0	1	1	0	0	0	0	0	0	0	0

Note: 1 means the DOF is coupled to the corresponding RP, while 0 means uncoupled.
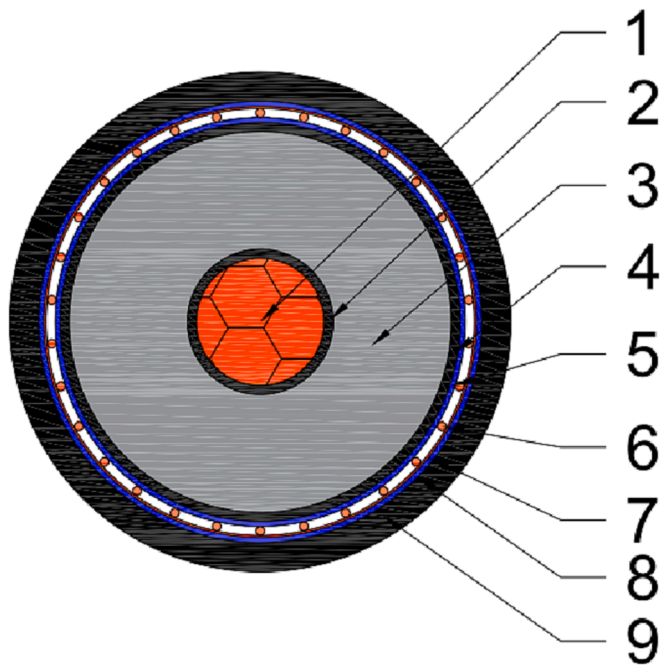

Fig. 9. Cross section of the submarine power cable.

Table 2
Parameters of the cable specimens.

Layer	Component	Thickness (mm)	Outer diameter (mm)	Materials
1	Copper conductor	–	11.4	Copper
2	Conductor shield	0.8	13.0	XLPE
3	Insulation	10.5	34.0	XLPE
4	Insulation shield	1.0	36.0	XLPE
5	Water-proof layer	0.45	36.9	XLPE
6	Copper wire	1.15	39.2	Copper
7	Copper shield	0.2	39.6	MDPE
8	Water-proof layer	0.45	40.5	MDPE
9	Sheath	2.5	45.5	MDPE

$$A_{lt}^{C} = \begin{cases} -1 & l = t \\ 0 & l \neq t \leqslant 3 \\ -\partial R(\phi^{C})(X^{B} - X^{C} + U^{A})/\partial U_{t}^{C} & t > 3 \end{cases} \qquad (15)$$

where $l = 1,2,3$ and $t = 1, …, 6. R(\phi^{C})$ has to be given in order to obtain $\mathbf{A}^{A}$ and $\mathbf{A}^{C}$. Based on Krenk, S. et al. [28], $R(\phi^{C})$ can be obtained through the quaternion parameter representation of a rotation φ about its rotation axis n consisting of a scalar r_0 and a vector $\mathbf{r}$, defined by:
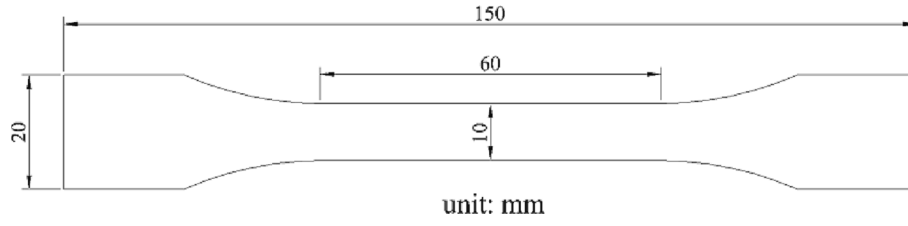
Fig. 10. The detailed dimensions of MDPE & XLPE.

Fig. 11. Dumbbell shape of MDPE (left) & XLPE (right).

$$r_0 = \cos(\frac{1}{2}\varphi), \mathbf{r} = \sin(\frac{1}{2}\varphi)\mathbf{n} \qquad (16)$$

In full matrix form, the rotation representation is:

$$\mathbf{R} = \begin{bmatrix} r_0^2 + r_1^2 - r_2^2 - r_3^2 & 2(r_1 r_2 - r_0 r_3) & 2(r_1 r_3 + r_0 r_2) \\ 2(r_1 r_2 + r_0 r_3) & r_0^2 - r_1^2 + r_2^2 - r_3^2 & 2(r_2 r_3 - r_0 r_1) \\ 2(r_1 r_3 - r_0 r_2) & 2(r_2 r_3 + r_0 r_1) & r_0^2 - r_1^2 - r_2^2 + r_3^2 \end{bmatrix} \qquad (17)$$

The coefficients in Eq. (13) and Eq. (15) thus can be obtained.

2.2. Implementation of RUC technique in FEM

Following the overview of the fundamental principles of the RUC technique, this section focuses on its implementation in the ABAQUS/Standard finite element software package. It covers various aspects such as element selection, interaction modelling, algorithm implementation, boundary conditions, and loading strategies.

2.2.1. Element & interaction

C3D8R (An 8-node linear brick, reduced integration, hourglass control) is chosen to mesh the cable for all the components. In order to obtain the variables in the wire axial direction, a local discrete coordinate system that follows the winding direction of each helical wire is hence defined in ABAQUS, as shown in Fig. 7. 1 is the wire axial direction, 2 is the tangential direction while 3 is defined through the right-hand rule.

Contact interactions among each component is a key factor affecting the final result and it is also the main source of the high computational cost and numerical instability, thus requiring careful selection of the tangential and normal interaction mechanisms. All the contact interactions among each component are taken into account. Surface-to-surface discretization method is used to model the contact between surfaces where both the tangential behaviour and normal behaviour employ penalty method. The contact stiffness is set to 2000 N/mm³ for optimally obtaining low CPU cost and enough contact solution accuracy while constant isotropic coulomb friction $\mu = 0.12$ is selected in the tangential direction in accordance with Caleyron, F., et al. & Lukassen, T.V., et al. [20,29].

2.2.2. Algorithm & loading strategy

The RUC model is implemented in the commercial software ABAQUS/Standard by using Standard/static algorithm in order to simulate
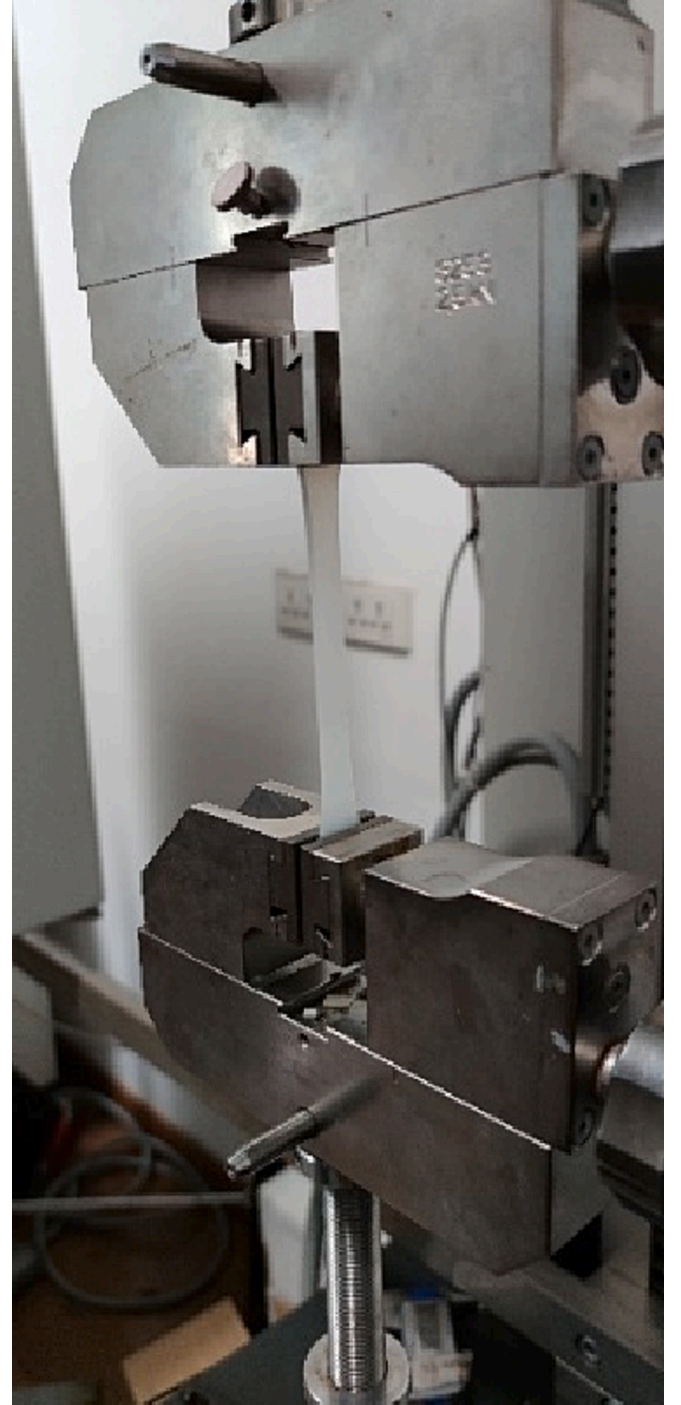

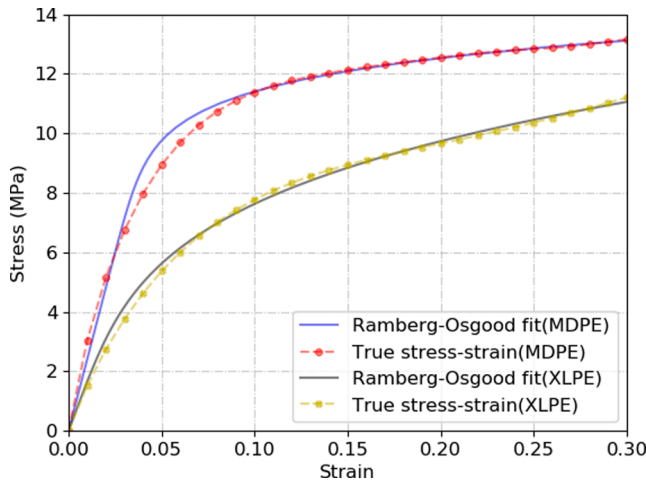**Fig. 12.** Tension test under an electronic universal testing machine.

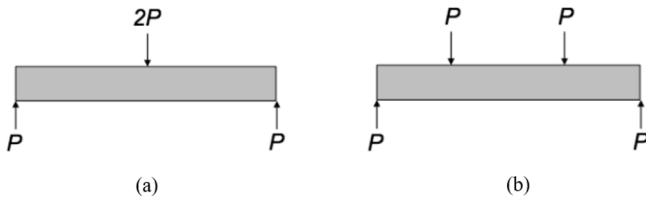**Fig. 13.** Ramberg-Osgood fit of MDPE and XLPE.

Fig. 14. (a) Three-point bending and (b) four-point bending.

the static process considering the loading process during the test is very slow. The points in the centreline of Layer I, as shown in Fig. 8, are defined to couple the DOFs belonging to the corresponding cross section. These points are corresponding to the points in Fig. 4. Three types of points are defined: Master, Slave & Symmetry point. The rest of the points that are not denoted in Fig. 8 are the slave points. The details of the coupling setup are given in Table 1. U3 and U4 DOFs of all the cross section nodes of Layer I are correspondingly coupled to all the centreline points. For Layer II and Layer IV, U3 and U4 DOFs on the most left and most right sides are coupled to master points, and meanwhile, all the DOFs of the symmetric cross section are coupled to the symmetry point. Finally, two opposite bending angles are applied on the ends of the cable.

3. Mechanical tests

The test is used to provide material properties and validate the curvature-moment relation from the RUC model. The test specimens in this paper are 35 KV alternative current power cables produced by

Oriental Cable (NBO). They are composed of nine layers, and their configuration as well as detailed manufacturing dimension are shown in Fig. 9 and Table 2.

In this section, the tests concerning the properties of the materials XLPE (cross-linked polyethylene) & MDPE (medium-density poly-ethylene) used in the cable sample and the bending behaviour of the cable sample are presented in Section 3.1 and Section 3.2, respectively.

3.1. Material test (MDPE & XLPE)

The cable investigated in this paper consists of nine layers, including a helical wire layer composed of 40 helical wires with a pitch length of 400 mm. The primary materials used in this cable design are copper for the conductor, copper wire, and copper shield, XLPE for the insulation layer, and MDPE for the outermost sheath. The copper material exhibits a Young's modulus of 90 GPa, a Poisson's ratio of 0.32, and a yield strength of 130 MPa. However, it is important to note that XLPE and MDPE materials may exhibit altered behaviour once extruded into cylindrical shapes. Consequently, material testing for XLPE and MDPE involved cutting test samples directly from the cable product to accurately capture their mechanical properties.

In order to obtain the strain–stress relation, according to ISO 527–2012 [30], MDPE and XLPE cut from cable samples were made into dumb-bell shape and have a dimension in Fig. 10. Both MDPE and XLPE have five samples, respectively, as shown in Fig. 11. The strains during the tension process were recorded by extensometers on an electronic universal test machine, as shown in Fig. 12. The test machine has a

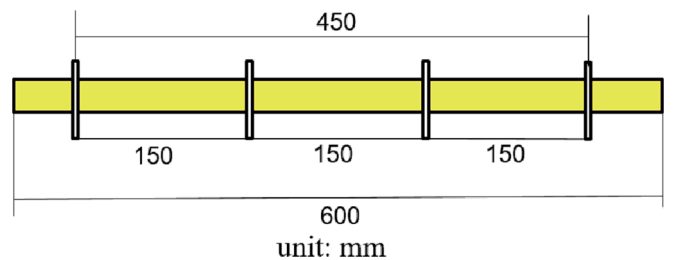**Fig. 16.** Cable specimens for bending test.

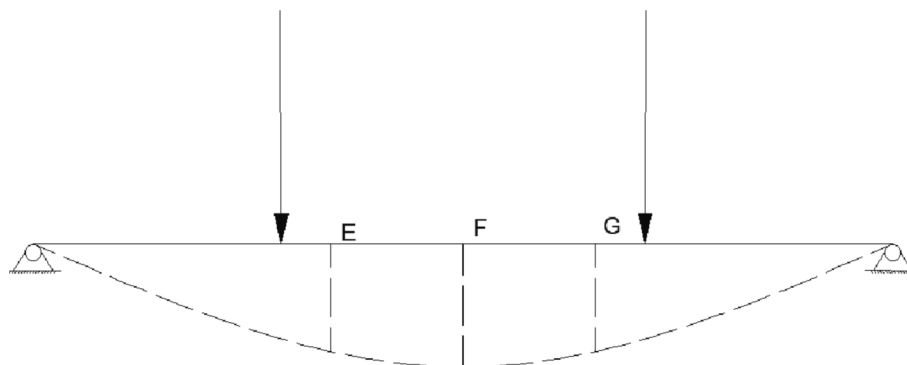**Fig. 17.** Dimension for the cable specimens.

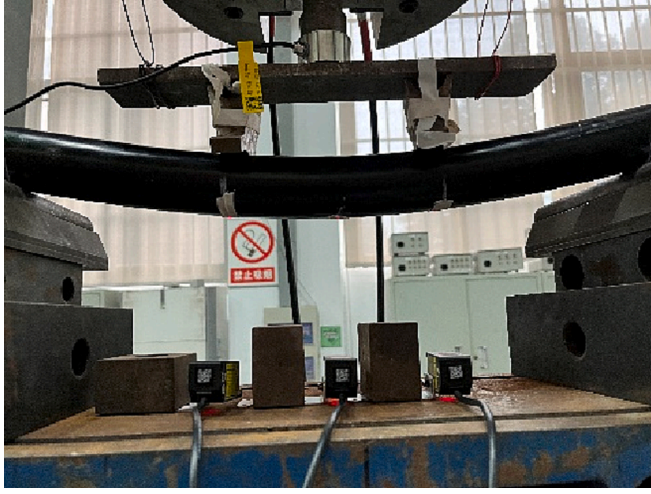**Fig. 15.** The sketch for the bending of a slender structure.

Fig. 18. Bending illustration of a cable sample.

measuring range of 2.5 KN, and the tension speed was controlled as 5 mm/min for all the samples.

After the test, the stress and strain relation of each sample can be obtained. Through the linear interpolation method and averaging process of the five samples of each material, the stress–strain relations can be obtained. The true stress and true strain are calculated according to:

$$\varepsilon_{True} = \ln(1 + \varepsilon_{Nominal}) \tag{18}$$

$$\sigma_{True} = \sigma_{Nominal}(1 + \varepsilon_{Nominal}) \tag{19}$$

To facilitate the manipulation in the numerical model, an expression for the true stress–strain relationship is generated via Ramberg-Osgood equation [31]. The total strain ε_t is the sum of the elastic strain ε_e and the plastic strain ε_p, which results in:

$$\varepsilon_t = \varepsilon_e + \varepsilon_p = \frac{\sigma}{E} + (\frac{\sigma}{K})^g \tag{20}$$

where σ is the stress, K the nonlinear modulus, g the hardening exponent, E the Young's modulus calculated as the secant modulus when the true strain is between 0.05% and 0.25% based on the standard ISO527-2012 [32]. The generated Ramberg-Osgood curves of the two types of material are shown in Fig. 13.

3.2. Bending test

The traditional techniques for the bending test of a slender structure can be a three-point bending or a four-point bending, as shown in

Fig. 14. A four-point bending test is adopted here regarding four cable samples until the their final curvatures reach $1e-3 \text{ mm}^{-1}$. In order to obtain the curvature, the vertical displacements at three spots should be paid attention to. As shown by points E, F and G in Fig. 15, three displacement sensors could be installed below them, and then the displacement of these three points could be captured for calculating the curvature. Since the curvature in the middle section is near constant, the three points we are interested in form a standard circle, based on which the curvature can be calculated. The general equation of a circle can be described by a quadratic polynomial:

$$A(x^2 + y^2) + Bx + Cy + D = 0 \tag{21}$$

The above equation can be transformed into the standard equation for a circle:

$$(x + \frac{B}{2A})^2 + (y + \frac{C}{2A})^2 = \frac{B^2 + C^2 - 4AD}{4A^2} \tag{22}$$

The coordinate of the three points: E(x₁,y₁), F(x₂,y₂) and G(x₂,y₂) are replaced into Eq. (22), then the coefficients for the circle can be obtained. The bending radius of the cable R_B is:

$$R_B = \sqrt{\frac{B^2 + C^2 - 4AD}{4A^2}} \tag{23}$$

At last, the curvature is obtained:

$$\kappa = \frac{1}{R_B} \tag{24}$$

Fig. 16 shows the cable samples that were used in the bending test. Their lengths are 600 mm. The geometry size of the samples in the length direction is shown in Fig. 17. They are then placed on a four-point bending test facility, which has two supports to hold the cables and two loading rings to apply the bending on them, as shown in Fig. 18. The bending results are given and discussed in Section 5.

4. Full-Scale model

To compare with the RUC model, a full-scale model is built, as shown in Fig. 19. All the model information such as the geometry, material,

Table 3
Parameters and materials used in the simplified model.

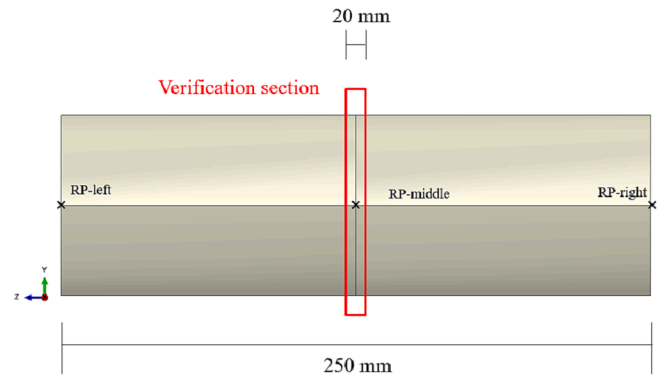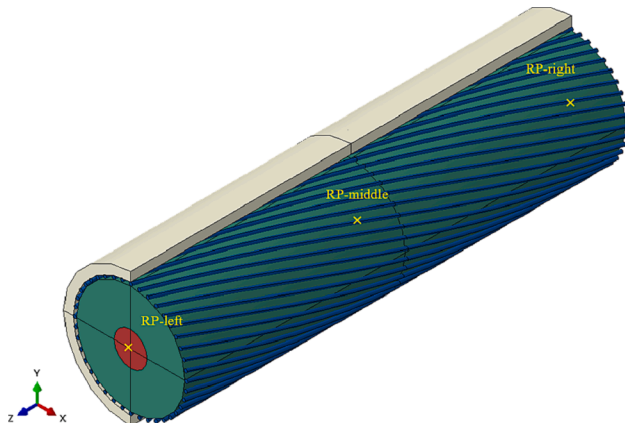| Layers	Thickness (mm)	Outer diameter (mm)	Materials
I	–	11.4	Copper
II	12.75	36.9	XLPE
III	1.15	39.2	Copper
IV	3.15	45.5	MDPE

Fig. 19. Full-scale model of the cable.
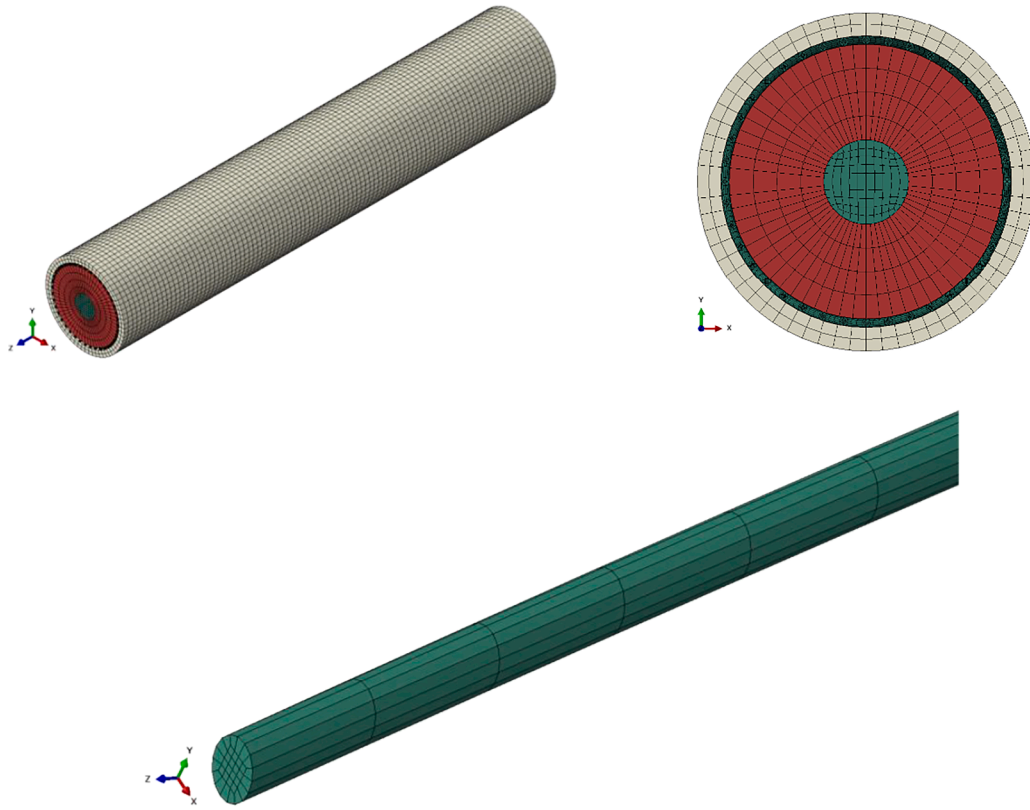
Fig. 20. Mesh result of the full-scale model.

Table 4
Coupling DOFs for the three RPs.

	RP-left & RP-right						RP-middle					
	U1	U2	U3	U4	U5	U6	U1	U2	U3	U4	U5	U6
Layer I	1	1	1	1	1	1	1	1	1	1	1	1
Layer II	1	1	1	1	1	1	0	0	1	1	1	0
Layer IV	1	1	1	1	1	1	0	0	1	1	1	0

algorithm and contact are the same as those in the RUC model, except that the length of the full model becomes 250 mm, 100 mm longer than the effective length of the test sample. The length is determined according to the rule that the model length is supposed to be 5 times longer than its diameter based on Paumier[24]. In this way, there are more 50 mm longer over both sides respectively, in order to eliminate the boundary effect as much as possible under available calculation resources.

According to the cross section in Fig. 9, in the 9 layers, a couple of layers are extremely thin compared to the other layers, which makes the contributions from these layers comparatively smaller. Therefore, the thin layers are combined into their neighbouring layers in order to simplify the numerical model. The simplified structure and the corresponding materials in each layer are shown in Table 3. Notice, even though the copper wires are not thick enough to contribute a lot, due to their special structure style, it is still of our interest to investigate their behaviour, therefore, the wires are kept originally in order to have a full study. In order to effectively compare with the RUC model, the middle section with the same length as RUC model will be cut out in the post process. The mesh result is given in Fig. 20, which contains 713,600 elements and 1,304,480 nodes in total.

The model is symmetric in the z direction as well, with three RPs in the centreline. These RPs are coupled to the corresponding nodes of Layer I, Layer II and Layer IV in the way listed in Table 4. Even though the model should be as long as possible to get rid of the boundary effect,

considering current computation capability, a super long model is not allowed and current full-scale model is not perfect. Both end sides are set as rigid surfaces to apply the bending on the cable, therefore, a short section in the middle will be cut out to compare with the RUC model in Section 5 to eliminate the boundary effect as much as possible. To enable the free movement among each layer, U1, U2 & U6 of the RP-middle to Layer II and Layer IV in the symmetric cross section are decoupled to free the nodes in these directions. The helical wire layer, however, is not restricted on both sides. They are able to move inside the cable freely with only the contact restrictions from the neighbouring layers, which is not the situation in the RUC model that simulates a super long power cable.

As for the boundary conditions, RP-middle is totally fixed. The nodes in the centreline of the inner conductor is fixed in U1, U5 and U6 directions. Finally, two opposite bending moment are applied on RP-left and RP-right.

5. Model validation & verification

Sections 2, 3 and 4 discuss RUC model, test and full-scale model of the cable under bending, respectively. Both the RUC model and the full-scale model are applied on the test cable. The RUC model has a length of 20 mm while the full-scale model has a length of 250 mm. The material and geometry properties used in the following case study are given in Section 3.1 in detail.
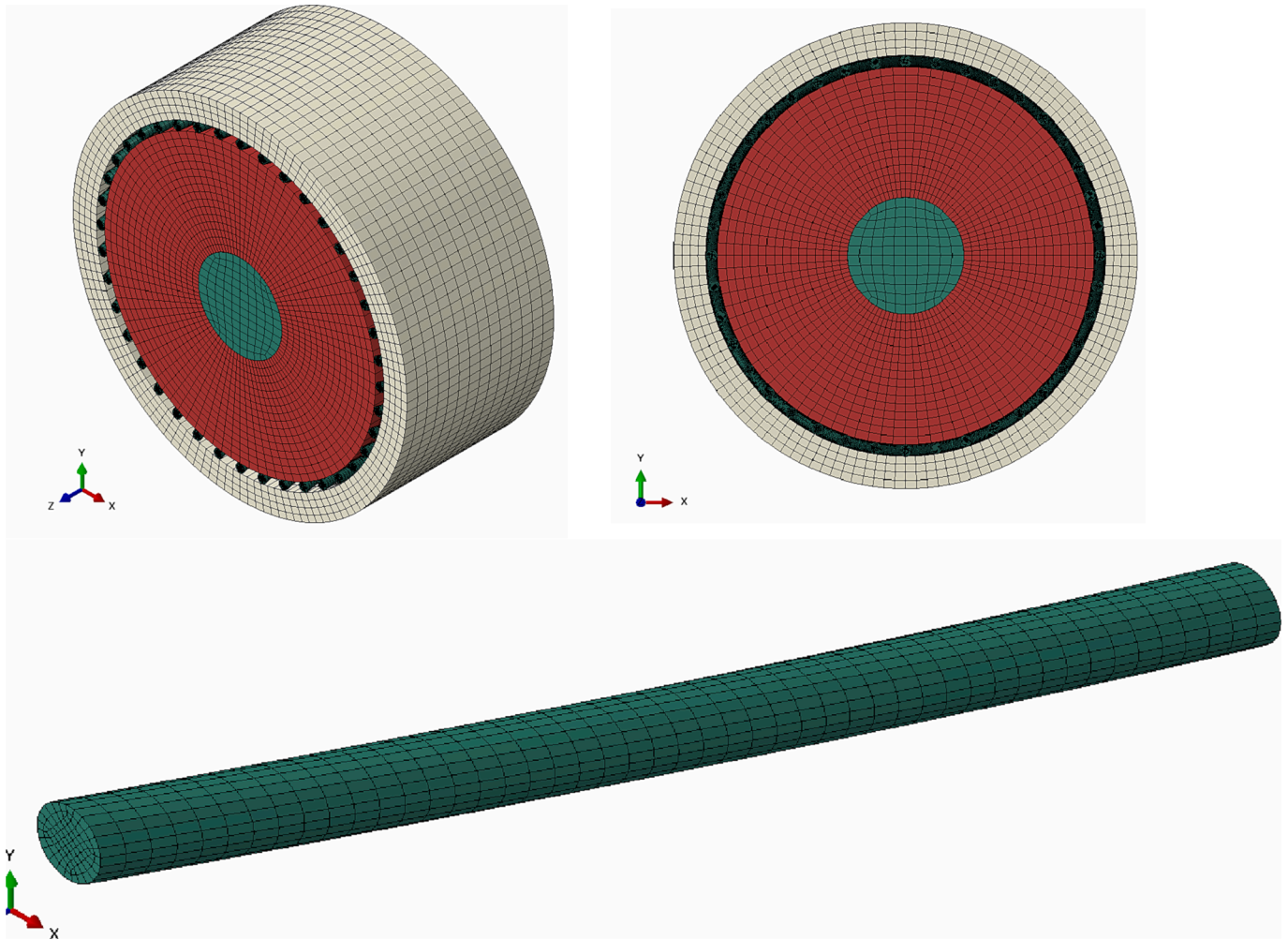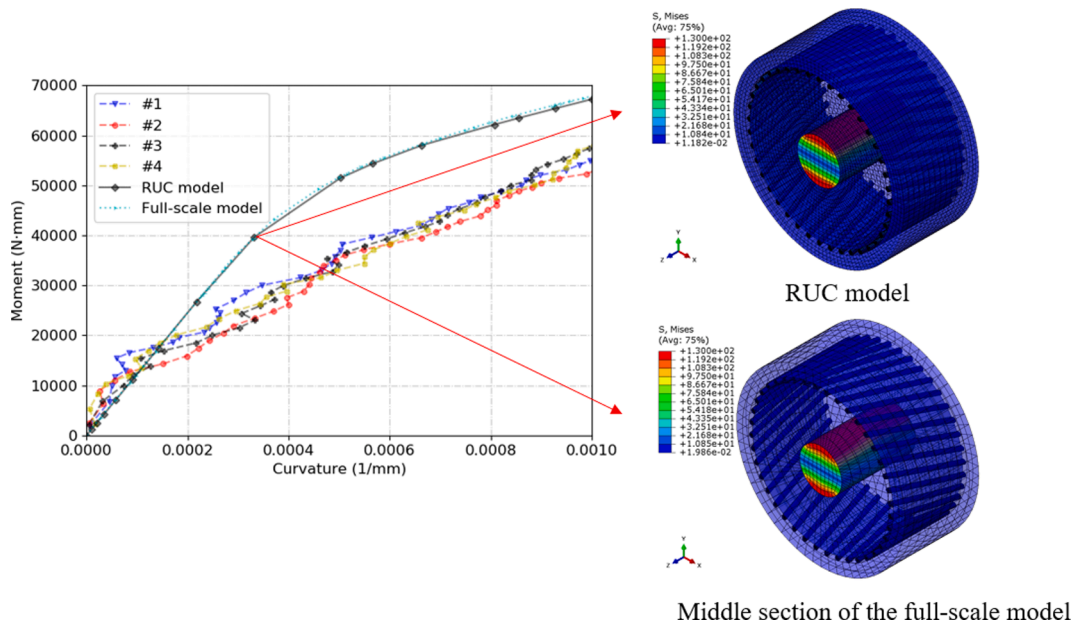
Fig. 21. Meshing of the RUC cable.

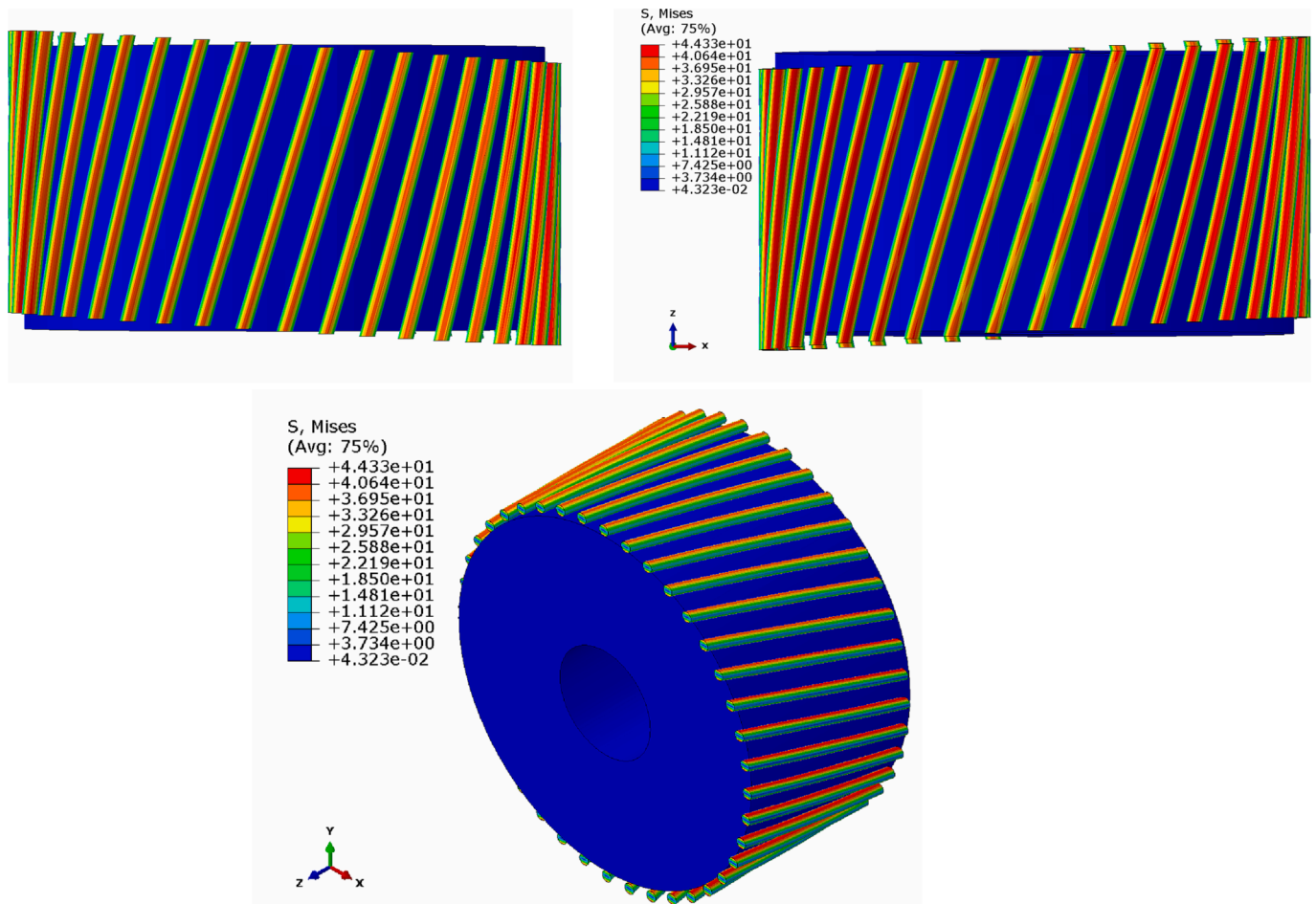**Fig. 22.** Curvature-bending moment relation from the test, RUC and the full-scale model.

Fig. 23. The movement of the helical wires relative to the inner layers at $\kappa_G = 1\mathrm{e} - 3\,\mathrm{mm}^{-1}$ from the RUC model.
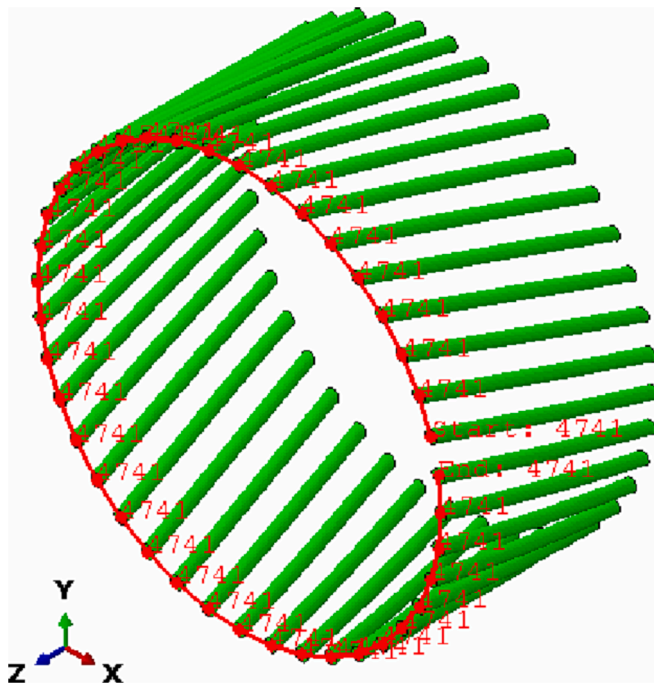

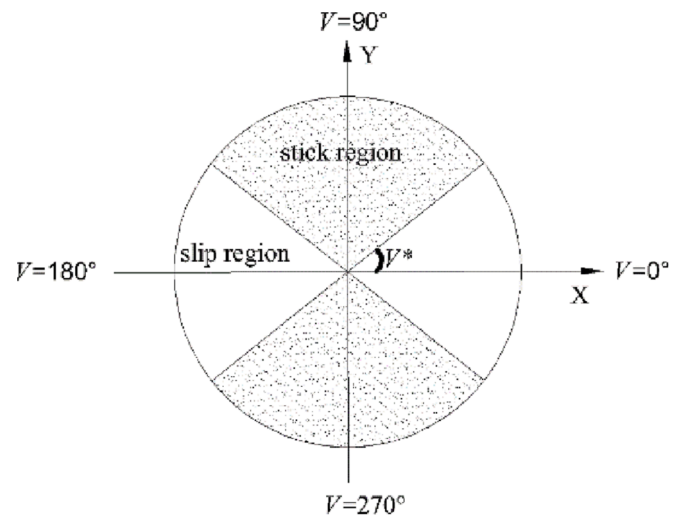**Fig. 24.** Node path along the left cross section.

Fig. 25. Stick and slip zones on a cross section.

The mesh results regarding the RUC cable and one of the wires are shown in Fig. 21. All the cylinder layers consist of 14 elements in the cable axial direction while the wire has 48 elements in the cable axial direction. This mesh strategy generates in total 990,455 nodes and 564,696 elements.

From the cable level, the curvature-moment relation from the RUC model is invalidated against test and verified through the full-scale
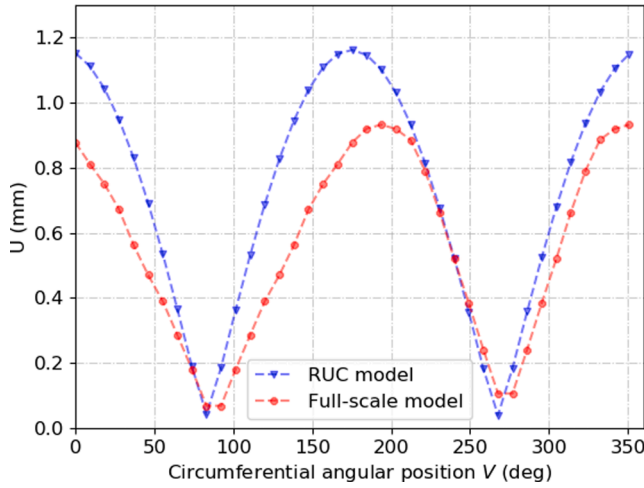
Fig. 26. The displacements of the nodes along the cross section at $\kappa_G = 1e - 3 \, \text{mm}^{-1}$ from RUC and full-scale model.

model in Section 5.1. From the component level, the stress and movement especially of the helical wire layer are discussed elaborately in Section 5.2.

5.1. Cable overall behaviour

Fig. 22 presents the curvature-bending moment curves from the experiment, RUC model and the full-scale model. All of the curves have the same trend. The moment increases with the increase of the curvature and it is observed that the slopes of the curves in the beginning phase are steeper than what is following.

The bending stiffness, i.e., the slope of the curve, from the RUC model and the full-scale FEM model agrees better with the test result at the beginning phase when the curvature is less than $0.13e - 3 \, \text{mm}^{-1}$. However, when the curvature overpasses this value, the bending moments from the two numerical models increase faster than the test result. The discrepancy might be caused by the slip issue among the cylinder layers. The original cable sample shown in Fig. 9 has 9 layers, but they are simplified into 4 layers in total, which ignores much slip issue. More importantly, the test samples have two end cross sections totally relaxed and the restrictions on both sides can be largely disregarded, whereas the boundary conditions in the numerical models are not the same. Therefore, as the curvature increases, the moments from the two FEM models become higher than the test results, with an error near 14% between RUC model and test results when the curvature reaches $1e - 3 \, \text{mm}^{-1}$. However, one of the main reasons to cause the moment decrease in all the methods is the material nonlinearity. As the slope of the curve from the RUC model starts to decrease exactly when the

copper in Layer I reaches its nonlinear phase, as shown in Fig. 22.

Another phenomenon observed is that the results from the RUC model and the full-scale FEM model agree with each other quite well, with only 1.7% error regarding the moment when the curvature reaches $1e - 3 \, \text{mm}^{-1}$. At this moment, Mises stress of most of Layer I cross section has reached copper's yield strength. The helical wires already slip far away from their original places. Even the mesh from the RUC model is denser than the full FEM model, the calculation time to finish the RUC model is only 60 min with 16 CPU cores. However, the calculation time for the full FEM model costs near 210 min with 32 CPU cores. Besides, the RUC model presents better convergence compared with the full FEM model.

5.2. Component behaviour

Fig. 23 presents the movement of the helical wires relative to the inner neighbouring layer when the curvature reaches $\kappa_G = 1e - 3 \, \text{mm}^{-1}$. The helical wires have witnessed quite obvious slip, especially the wires on the neutral plane, while the counterparts on the intrados and extrados of the cable hardly slip. This phenomenon fits the analytical model proposed by Papailiou[33] where the slip first appears near the neutral plane of the cable and extends to the intrados and extrados. In order to investigate the displacement of the nodes along the circumferential angular position, The path is created by stringing the centre node of each wire on the same cross section together, as illustrated in Fig. 24. The path is from $V = 0$ to $V = 360$ deg illustrated in Fig. 25. The magnitudes of the displacement of the nodes along the cross section are then given in Fig. 26 regarding both the RUC model and the full-scale model, which shows that the displacements of the nodes near the cable neutral axis, i.e. $V = 0$ deg, are the largest, and the displacement gradually decreases to almost 0 near the extrados and intrados. This is also observed by the U contor plot in Fig. 27. However, it can also be observed that the highest value near the neutral plane of the cable has a discrepancy between these two numerical models. The RUC model gives a value 23.9% higher than that from the full-scale model. This can be explained by the fact that the boundary conditions of the helical wire layer in the full-scale model are totally free, whereas the helical wire layer is set as the periodic boundary conditions. These added boundary conditions are used to reflect the mechanical behaviour of a super long cable in practical situations where the helical wires are restricted on the boundary sides.

Noteworthy, the materials exhibit serious nonlinear behaviour when the curvature of the cable surpasses $0.2e - 3 \, \text{mm}^{-1}$, therefore, the comparison in the following discussion will be focused on the behaviour before this curvature. The distribution of the stresses in the local X1-direction of all the wires is given in Fig. 28 under a global curvature $\kappa_G = 0.2e - 3 \, \text{mm}^{-1}$. No significant stress concentration is observed due to boundary effects and the stress looking from one side is basically all tension while the one on the other side is compression, which is induced
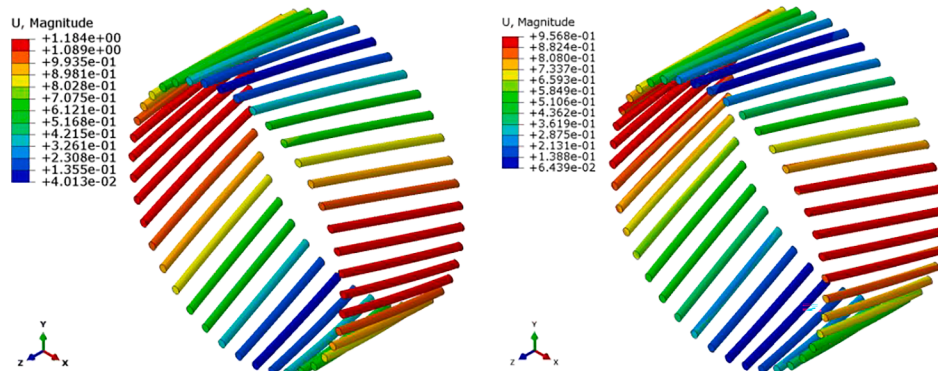

Fig. 27. The displacement distribution along the wires at $\kappa_G = 1e - 3 \, \text{mm}^{-1}$ from the RUC model (left) & full-scale model (right).
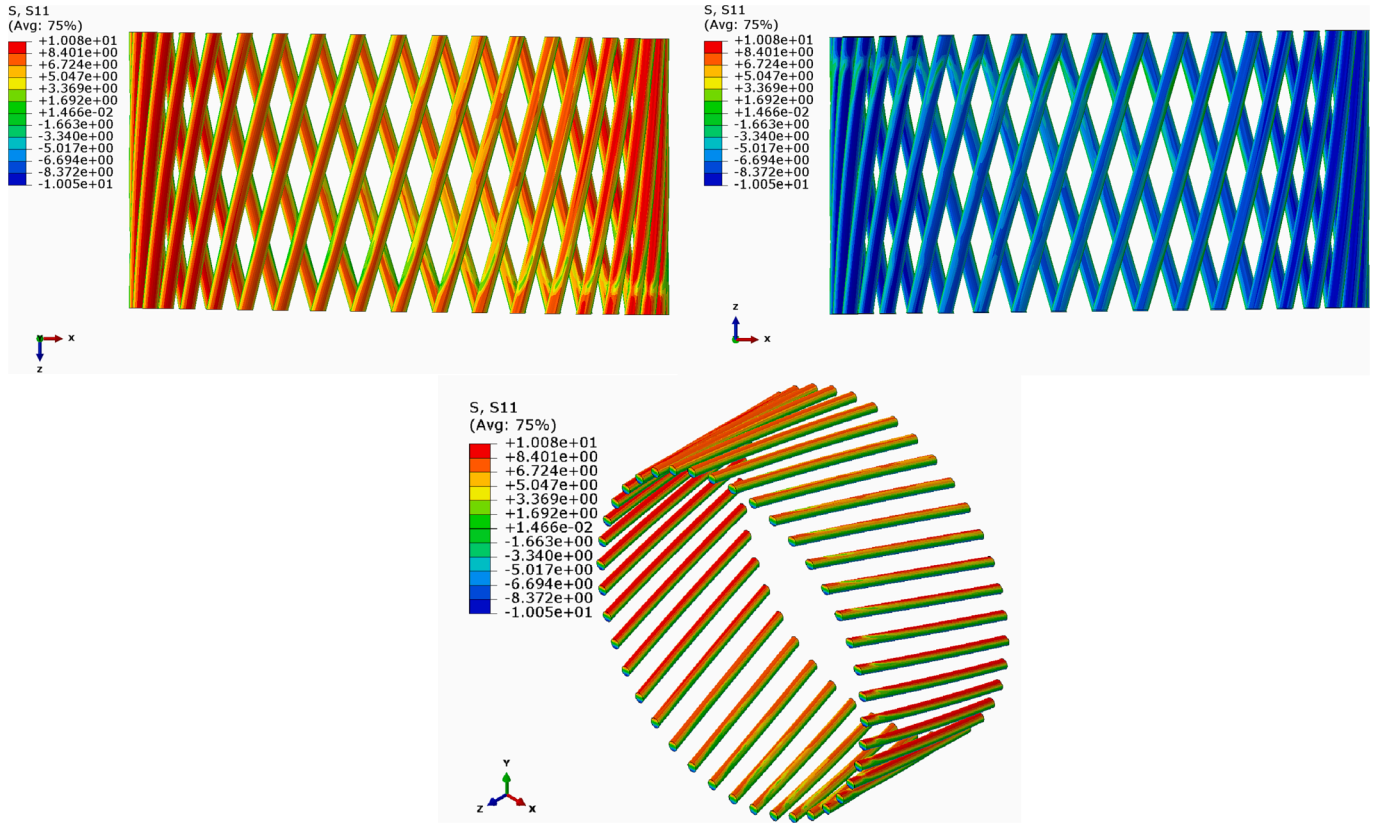
Fig. 28. Contour plot of stress of wires in X1-direction for $\kappa_G = 0.2\mathrm{e}-3\,\mathrm{mm}^{-1}$ from the RUC model.
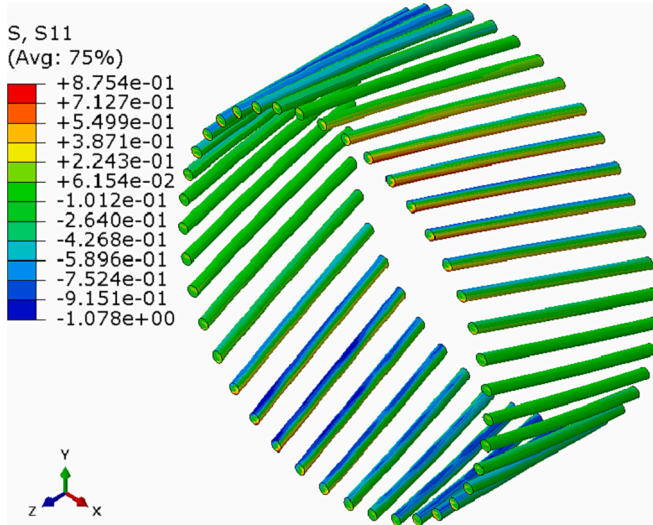

Fig. 29. Contour plot of stress of wires in X1-direction for $\kappa_G = 0.2\mathrm{e}-3\,\mathrm{mm}^{-1}$ from the full-scale model.

by the geometry deformation of the wires about their own neutral plane. The axial tension stress distribution of all the wires from the full-scale model, as given in Fig. 29, however, is much smaller than that from the RUC model. This is because that both sides of the helical wire layers are totally free in the full-scale model and there is no other restriction about them except the contact. The helical wires are able to slip away easily in the model. In order to reasonably compare with the RUC model regarding the axial tension stress of the helical wires, a super long model should be built with restrictions on both sides of the helical wire layer.

However, the calculation is hard to finish for this super long model considering current computation ability.

6. Conclusions

In this study, an RUC model for predicting the bending stiffness of SPCs is presented. The model is validated from the cable level through bending tests by studying the curvature-bending moment relations. Additionally, a full-scale numerical model is constructed to further verify the RUC model by examining the behaviour of the components. The developed RUC model holds potential for conducting bending studies on SPCs, and the key findings of this study can be summarized as follows:

1) The bending stiffness predicted by the RUC model agrees well with that from the full-scale model. They are validated against the test results with explainable error.
2) The bending stiffness from the RUC model and the tests is close to each other in the beginning phase. However, in the later phase, the stiffness from the test is smaller than the predicted. This is because the components are more easily to slip without restrictions on both sides during the test.
3) A dominant reason to cause the decrease of the bending stiffness in all the methods is the material nonlinearity. It is observed from the RUC model that the stiffness starts to change when the material copper overpasses its elasticity.
4) The magnitudes of the displacement of the wires are largest near the neutral plane of the cable and decrease to the smallest near the extrados and intrados.

In conclusion, the paper demonstrates the effectiveness of the proposed RUC model in handling SPCs under pure bending conditions. However, in practical engineering, SPCs often experience combined

loadings. The current focus of this paper is primarily on the fundamental development of the RUC model, and as such, combined tension and bending scenarios are not addressed. Nevertheless, the study highlights the potential of the RUC model to tackle SPCs under combined loadings, and this aspect will be explored in our further research.

Declaration of Competing Interest

The authors declare the following financial interests/personal relationships which may be considered as potential competing interests: [Pan Fang reports financial support was provided by China Scholarship Council [grant number 201906320047]].

Data availability

The data that has been used is confidential.

Acknowledgment

References

[1] water, D., *European Wind Energy Association.* 2013.
[2] 40, C.W.G.B., *TB 610—Offshore Generation Cable Connections.* 2015, CIGRE Paris, France.
[3] Marta, M., et al., *Development of dynamic submarine MV power cable design solutions for floating offshore renewable energy applications.* 2015.
[4] Fang P, et al. Mechanical responses of submarine power cables subject to axisymmetric loadings. Ocean Eng 2021;239:109847.
[5] Chang H-C, Chen B-F. Mechanical behavior of submarine cable under coupled tension, torsion and compressive loads. Ocean Eng 2019;189:106272.
[6] STANDARD, B. and B. ISO, *Petroleum and natural gas industries—Design and operation of subsea production systems—.* gas industries, 2006. **13628**: p. 10.
[7] DNV, *DNV, 2012, "Electrical Power Cables in Subsea Applications" DNV-RP-F401.* 2012.
[8] Lu H, Vaz MA, Caire M. A finite element model for unbonded flexible pipe under combined axisymmetric and bending loads. Mar Struct 2020;74:102826.
[9] Vaz M, et al. Experimental determination of axial, torsional and bending stiffness of umbilical cables. in *Proceedings of the 17th International Offshore & Arctic Engineering Conference (OMAE'98).* 1998.
[10] Ekeberg, K.I. and M.M. Dhaigude. Validation of the loxodromic bending assumption using high-quality stress measurements. in The 26th International Ocean and Polar Engineering Conference. 2016. International Society of Offshore and Polar Engineers.
[11] Coser, T.B., et al. Submarine power cable bending stiffness testing methodology. in The 26th International Ocean and Polar Engineering Conference. 2016. OnePetro.
[12] Sævik S. Comparison between theoretical and experimental flexible pipe bending stresses. in *International Conference on Offshore Mechanics and Arctic Engineering.* 2010.
[13] Cartraud P, Messager T. Computational homogenization of periodic beam-like structures. Int J Solids Struct 2006;43(3–4):686–96.
[14] Boso DP, Lefik M, Schrefler BA. A multilevel homogenised model for superconducting strand thermomechanics. Cryogenics 2005;45(4):259–71.
[15] Kamiński M, Schrefler B. Probabilistic effective characteristics of cables for superconducting coils. Comput Methods Appl Mech Eng 2000;188(1–3):1–16.
[16] Buannic N, Cartraud P. Higher-order effective modeling of periodic heterogeneous beams. I. Asymptotic expansion method. Int J Solids Struct 2001;38(40–41): 7139–61.
[17] Rahmati M, Bahai H, Alfano G. An accurate and computationally efficient small-scale nonlinear FEA of flexible risers. Ocean Eng 2016;121:382–91.
[18] Rahmati M, Alfano G, Bahai H. Small-scale FE modelling for the analysis of flexible risers. American Society of Mechanical Engineers; 2015.
[19] Rahmati M, Alfano G, Bahai H. Periodic and fixed boundary conditions for multi-scale finite element analysis of flexible risers. American Society of Mechanical Engineers; 2016.
[20] Caleyron F, et al. A multi-purpose finite element model for flexible risers studies. American Society of Mechanical Engineers; 2014.
[21] Leroy J-M, et al. Stress assessment in armour layers of flexible risers. in *International Conference on Offshore Mechanics and Arctic Engineering.* 2010.
[22] Lukassen TV, et al. Tension-bending analysis of flexible pipe by a repeated unit cell finite element model. Mar Struct 2019;64:401–20.
[23] Leroy J-M, et al. Assessing mechanical stresses in dynamic power cables for floating offshore wind farms. American Society of Mechanical Engineers Digital Collection; 2017.
[24] Paumier L, Averbuch D, Felix-Henry A. Flexible pipe curved collapse resistance calculation. in *International Conference on Offshore Mechanics and Arctic Engineering.* 2009.
[25] Li X, Jiang X, Hopman H. Curvature effect on wet collapse behaviours of flexible risers subjected to hydro-static pressure. Ships and Offshore Structures 2022;17(3): 619–31.
[26] Diehl, T., *Formulation of a User MPC to Simulate Beam-Type Transport Problems.* 1993, MFSP Internal Report, Department of Mechanical Engineering, University of ….
[27] Abaqus V. 6.14 Documentation. Dassault Systemes Simulia Corporation 2014;651: p. 6.2.
[28] Krenk, S., *Non-linear modeling and analysis of solids and structures.* 2009: Cambridge University Press.
[29] Lukassen TV, et al. Comparison between stress obtained by numerical analysis and in-situ measurements on a flexible pipe subjected to in-plane bending test. American Society of Mechanical Engineers; 2016.
[30] ISO, B., *Plastics-Determination of Tensile Properties.* 2012, ISO 527-2012.
[31] Ramberg, W. and W.R. Osgood, *Description of stress-strain curves by three parameters.* 1943.
[32] 527-2012, I., *Plastics-Determination of Tensile Properties,1-11.12.* 2012.
[33] Papailiou, K.O., *Bending of helically twisted cables under variable bending stiffness due to internal friction, tensile force and cable curvature.* Doctor of Technical Sciences thesis, ETH, Athens, Greece, 1995.